Available online at www.sciencedirect.com
SCIENCE DIRECT®
Journal of Computational Physics 201 (2004) 665–684
JOURNAL OF COMPUTATIONAL PHYSICS
www.elsevier.com/locate/jcp

On the elimination of numerical Cerenkov radiation in PIC simulations ☆

Andrew D. Greenwood *, Keith L. Cartwright, John W. Luginsland [1], Ernest A. Baca

Air Force Research Laboratory, Directed Energy Directorate, 3550 Aberdeen Ave SE, Kirtland, AFB NM 87117-5776, USA

Received 18 February 2004; received in revised form 22 June 2004; accepted 23 June 2004
Available online 25 August 2004

Abstract

Particle-in-cell (PIC) simulations are a useful tool in modeling plasma in physical devices. The Yee finite difference time domain (FDTD) method is commonly used in PIC simulations to model the electromagnetic fields. However, in the Yee FDTD method, poorly resolved waves at frequencies near the cut off frequency of the grid travel slower than the physical speed of light. These slowly traveling, poorly resolved waves are not a problem in many simulations because the physics of interest are at much lower frequencies. However, when high energy particles are present, the particles may travel faster than the numerical speed of their own radiation, leading to non-physical, numerical Cerenkov radiation. Due to non-linear interaction between the particles and the fields, the numerical Cerenkov radiation couples into the frequency band of physical interest and corrupts the PIC simulation. There are two methods of mitigating the effects of the numerical Cerenkov radiation. The computational stencil used to approximate the curl operator can be altered to improve the high frequency physics, or a filtering scheme can be introduced to attenuate the waves that cause the numerical Cerenkov radiation. Altering the computational stencil is more physically accurate but is difficult to implement while maintaining charge conservation in the code. Thus, filtering is more commonly used. Two previously published filters by Godfrey and Friedman are analyzed and compared to ideally desired filter properties.

☆ This work was supported by funding from the Air Force Office of Scientific Research (AFOSR).
* Corresponding author. Tel.: +1 505 846 6642; fax: +1 505 846 9103.
E-mail address: agreenwood@ieee.org (A.D. Greenwood).
[1] John W. Luginsland was with Air Force Research Laboratory, Directed Energy Directorate. He is now with NumerEx, Ithaca, NY.

0021-9991/$ - see front matter © 2004 Elsevier Inc. All rights reserved.
doi:10.1016/j.jcp.2004.06.021

1. Introduction

The electromagnetic fields in many particle-in-cell (PIC) simulations are computed using the finite difference time domain (FDTD) method first introduced by Kane Yee [1–3]. The Yee FDTD method is a very simple, robust tool for electromagnetic simulation; however, it is also known to suffer from anisotropic numerical phase error. This numerical dispersion error causes the numerical wave propagation speed to be slower than the physical wave propagation speed. The error is small at low frequency, becomes more severe at higher frequency and is most severe near the highest frequency supported by the computational grid. Thus, in purely electromagnetic simulations (i.e., simulations without charged particles), a grid with sufficiently small cells relative the the wavelengths of interest keeps the error at an acceptable level. However, when high-energy particles enter a PIC simulation, the situation changes drastically.

High-energy particles cause problems because, while their velocities cannot exceed the physical propagation speed of electromagnetic waves, they may exceed the numerical wave propagation speed, particularly near the highest frequency supported by the computational grid. This results in the appearance of non-physical, numerical Cerenkov radiation. The high frequencies that give rise to numerical Cerenkov radiation are poorly resolved by the simulation, and the physics of interest are typically at much lower frequencies. However, because of the nonlinear interaction between the particles and the electromagnetic fields, the numerical Cerenkov radiation couples into the frequencies of interest and corrupts the simulation. Thus, for a physically accurate PIC simulation, the numerical Cerenkov radiation must be eliminated.

There are two methods of dealing with numerical Cerenkov radiation. First, the computational stencil used to approximate the curl operator in the Yee FDTD method can be changed, resulting in new (and possibly improved) numerical dispersion characteristics. Second, a filter can be added to the Yee FDTD method to attenuate high-frequency waves, slowing or eliminating the growth of the numerical Cerenkov radiation. The second method is more common with the methods published by Godfrey [4], Friedman [5] and Rambo et al. [6] being examples of filtering to remove numerical Cerenkov radiation.

The remainder of this paper compares and contrasts various methods of eliminating numerical Cerenkov radiation in PIC simulations. Section 2 gives some background on the dispersion relation of the Yee FDTD method and shows the source of the numerical Cerenkov radiation. Section 3 introduces the concept of changing the computational stencil for the curl operator and gives examples of improved numerical dispersion characteristics. Section 4 introduces the idea of filtering and provides a suggestion for the ideal filter. The previously introduced Godfrey and Friedman filters are analyzed and compared, and numerical examples are given. A literature search failed to find a detailed numerical analysis of the Godfrey scheme; the dispersion relation of the Friedman scheme is first given in [7]. The general analysis of Section 4 facilitates the direct comparison of the different schemes. Section 5 wraps up with a conclusion.

2. Yee FDTD background

The Yee FDTD method employs a cubic lattice of cells to approximate Maxwell's curl equations, given by:

$$\begin{aligned} \frac{\partial \mathbf{B}}{\partial t} &= -\nabla \times \mathbf{E}, \\ \frac{\partial \mathbf{E}}{\partial t} &= c^2 \nabla \times \mathbf{B} - \eta c \mathbf{J}, \end{aligned} \tag{1}$$

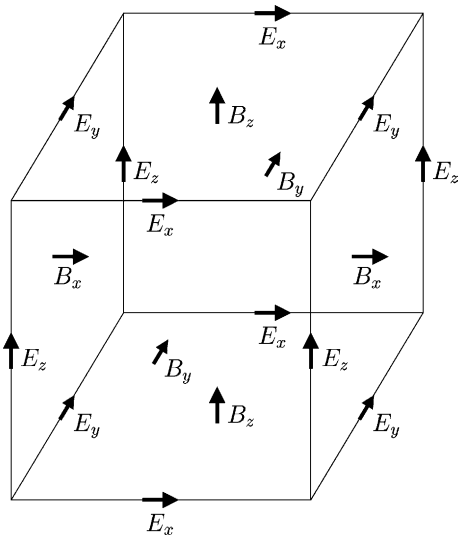

Fig. 1. Placement of the field components in the Yee FDTD method.

where c is the speed of light in the medium and η is the wave impedance. It achieves second order accuracy by staggering the placement of **E** and **B** in both space and time and approximating all derivative operators by centered finite differences. The electric fields (**E**) are placed on cell edges and the magnetic flux densities (**B**) are placed on cell faces, as shown in Fig. 1, and the electric fields are known at timesteps $n\Delta_t$ while the magnetic flux densities are known at timesteps $(n + 1/2)\Delta_t$.

In the Yee FDTD grid, electromagnetic waves propagate according to the dispersion relation

$$\left[\frac{1}{c\Delta_t}\sin\left(\frac{\omega\Delta_t}{2}\right)\right]^2 = \left[\frac{1}{\Delta_x}\sin\left(\frac{k_x\Delta_x}{2}\right)\right]^2 + \left[\frac{1}{\Delta_y}\sin\left(\frac{k_y\Delta_x}{2}\right)\right]^2 + \left[\frac{1}{\Delta_z}\sin\left(\frac{k_z\Delta_x}{2}\right)\right]^2, \tag{2}$$

where ω is the radian time frequency, and k_x, k_y, and k_z are the wavenumbers of the propagation parallel to the associated coordinate directions. In contrast, electromagnetic waves in real, physical space propagate according to

$$\frac{\omega^2}{c^2} = k_x^2 + k_y^2 + k_z^2 = k^2. \tag{3}$$

The Yee FDTD dispersion relation is seen to approximate the physical dispersion relation (Eq. (3)) at low frequency as shown in Fig. 2. Note that the numerical dispersion relation approximates the physical dispersion relation exactly up to the highest frequency the grid can support when the wave propagation is along a three dimensional (3D) diagonal of the grid and $\Delta_t = \Delta_{t,\max}$. For all other directions of propagation and timesteps, the propagation speed becomes slower than the physical speed of light (c) at high frequency. If charged particles travel at $0.8c$ in the simulation, note that the wave dispersion curves cross the particle speed line at high frequency, indicating the presence of numerical Cerenkov radiation. Note that the axes in Fig. 2 are normalized to Δ, indicating that the problem cannot be alleviated by refining the grid.

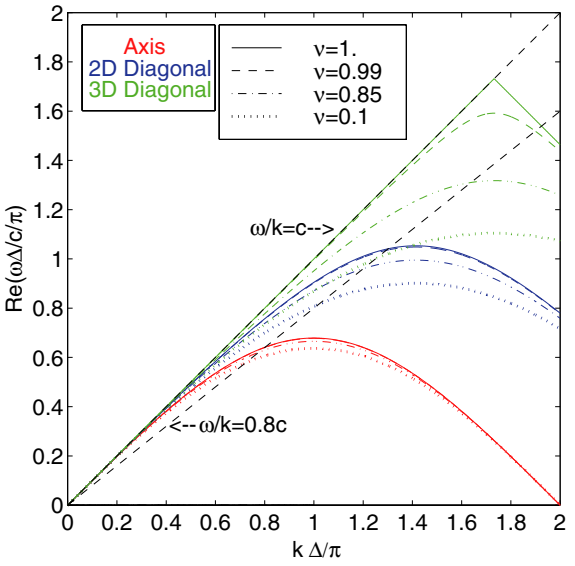

Fig. 2. Yee FDTD numerical dispersion relation for propagation along a grid axis, a 2D grid diagonal, and a 3D grid diagonal compared to the physical dispersion relation. The FDTD parameters are $\Delta_x = \Delta_y = \Delta_z = \Delta$ and $\Delta_t = v\Delta_{t,\max} = v\Delta/c/\sqrt{3}$.

3. Altering the computational stencil

Altering the computational stencil involves changing the approximation to the spatial derivatives for the FDTD method. The standard Yee FDTD method uses second order centered finite differences to approximate all spatial derivatives. Thus $\nabla \times \mathbf{E}$ to update the B_z value at the center if Fig. 3 is computed using the E_x and E_y values shown in green as

$$\hat{z} \cdot (\nabla \times \mathbf{E})_{I+1/2,J+1/2,K} = \frac{E_{y,I+1,J+1/2,K} - E_{x,I+1/2,J+1,K} - E_{y,I,J+1/2,K} + E_{x,I+1/2,J,K}}{\Delta} + \mathrm{O}(\Delta^2), \tag{4}$$

where the subscripts I, J, K indicate the quantity evaluated at $(I\Delta_x, J\Delta_y, K\Delta_z)$ and $\Delta_x = \Delta_y = \Delta_z = \Delta$ is assumed. The curl can also be approximated using the values shown in red as

$$\hat{z} \cdot (\nabla \times \mathbf{E})_{I+1/2,J+1/2,K} = \frac{E_{y,I+2,J+1/2,K} - E_{x,I+1/2,J+2,K} - E_{y,I-1,J+1/2,K} + E_{x,I+1/2,J-1,K}}{3\Delta} + \mathrm{O}(\Delta^2) \tag{5}$$

or using the values shown in blue as

$$\begin{aligned}\hat{z} \cdot (\nabla \times \mathbf{E})_{I+1/2,J+1/2,K} = \frac{1}{6\Delta}\big(&E_{y,I+2,J-1/2,K} + E_{y,I+2,J+3/2,K} - E_{x,I+3/2,J+2,K} - E_{x,I-1/2,J+2,K} - E_{y,I-1,J+3/2,K} \\ &- E_{y,I-1,J-1/2,K} + E_{x,I-1/2,J-1,K} + E_{x,I+3/2,J-1,K}\big) + \mathrm{O}(\Delta^2).\end{aligned} \tag{6}$$

Each of the above curl approximations is individually second order accurate. Thus, a linear combination is also second order accurate, and the curl is approximated by K_1 times Eq. (5) plus K_2 times Eq. (6) plus $(1 - K_1 - K_2)$ times Eq. (4) [8]. Note that useful values of K_1 and K_2 are $K_1 \leqslant 0$ and $K_2 = 0$ or $K_2 = 2K_1$. The case $K_1 = K_2 = 0$ recovers the standard Yee FDTD scheme, and the case $K_1 = -1/8$, $K_2 = 0$ results in a fourth order accurate approximation to the curl operator.

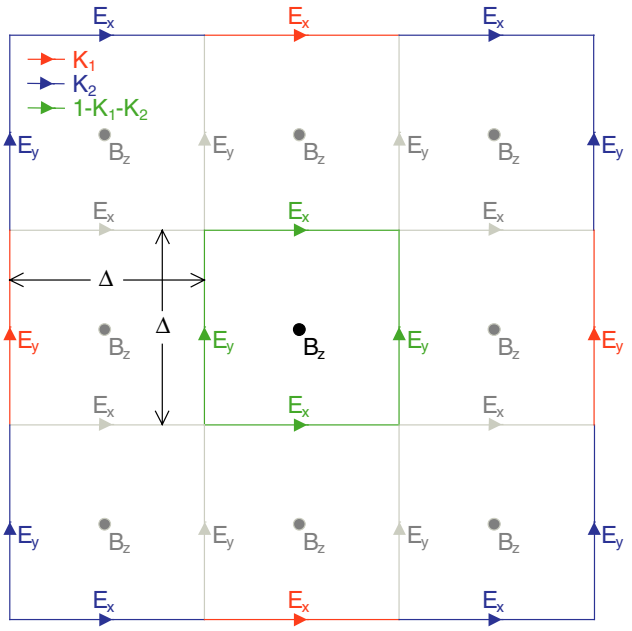

Fig. 3. E_x and E_y values used to compute $\nabla \times \mathbf{E}$ to update B_z. The standard Yee FDTD scheme uses the values shown in green. The values shown in red and blue can be used in addition to the values shown in green.

The dispersion relation for the extended stencil FDTD method is given by

$$\left[\frac{1}{c\Delta_t}\sin\left(\frac{\omega\Delta_t}{2}\right)\right]^2 = f_{x,y}f_{x,z} + f_{y,z}f_{y,x} + f_{z,x}f_{z,y}, \tag{7}$$

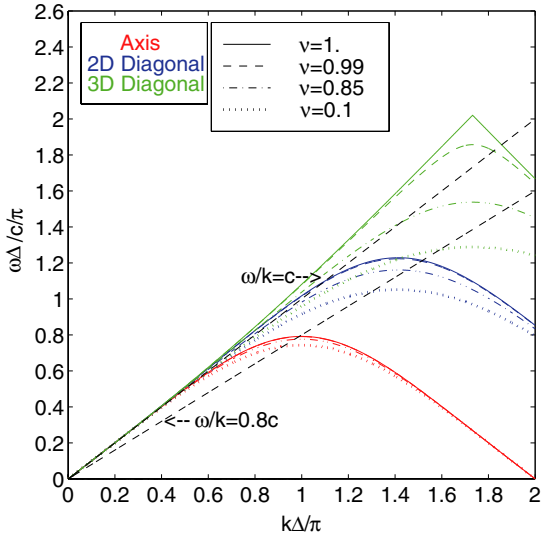

Fig. 4. Extended stencil numerical dispersion relation for $K_1 = -1/8$, $K_2 = 0$, $\Delta_x = \Delta_y = \Delta_z = \Delta$, and $\Delta_t = \nu\Delta_{t,\max} = (6/7)\nu\Delta/c/\sqrt{3}$.

where

$$f_{\alpha,\beta} = \frac{1}{\Delta_\alpha}\left\{[1 - K_1 - K_2]\sin\left(\frac{k_\alpha \Delta_\alpha}{2}\right) + \frac{1}{3}\left[K_1 + K_2\cos\left(k_\beta \Delta_\beta\right)\right]\sin\left(\frac{3K_\alpha \Delta_\alpha}{2}\right)\right\}. \tag{8}$$

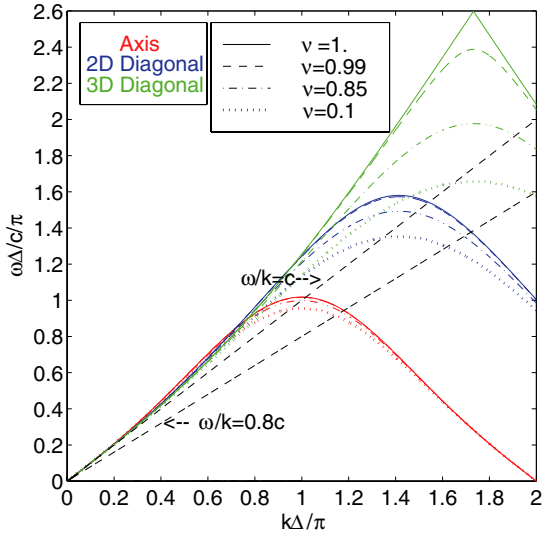

Fig. 5. Extended stencil numerical dispersion relation for $K_1 = -3/8,\ K_2 = 0,\ \Delta_x = \Delta_y = \Delta_z = \Delta,$ and $\Delta_t = \nu\Delta_{t,\max} = (2/3)\nu\Delta/c/\sqrt{3}$.

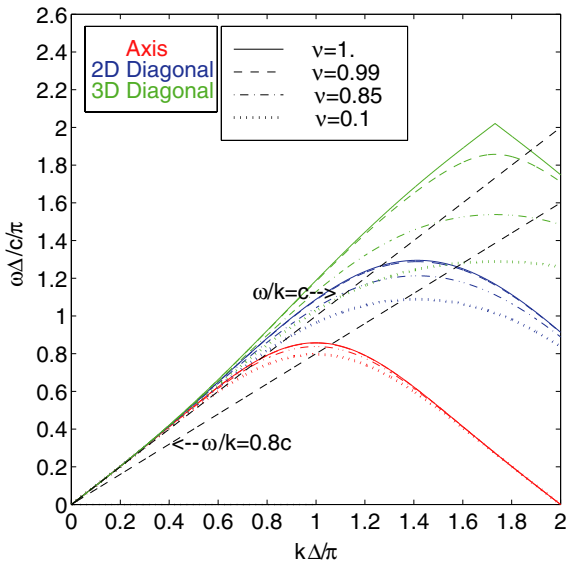

Fig. 6. Extended stencil numerical dispersion relation for $K_1 = -1/16,\ K_2 = 2K_1,\ \Delta_x = \Delta_y = \Delta_z = \Delta,$ and $\Delta_t = \nu\Delta_{t,\max} = (6/7)\nu\Delta/c/\sqrt{3}$.

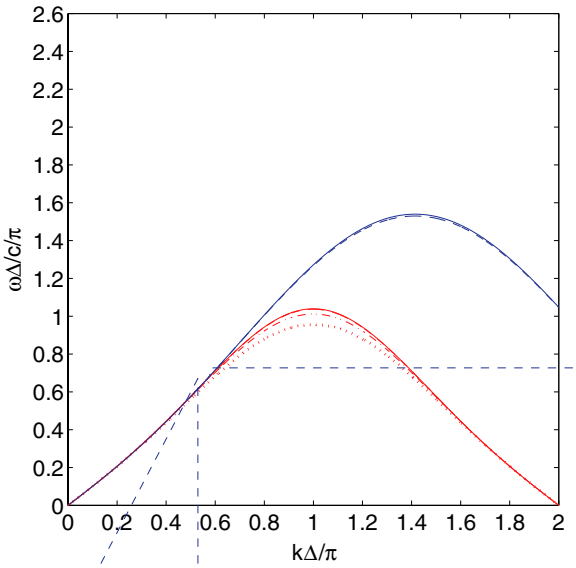

When $K_2 = 0$, the maximum stable timestep for the extended stencil method is $1/(1 - (4/3)K_1)$ times the maximum stable timestep for the standard Yee method. When $K_2 = 2K_1$, the maximum stable timestep is $1/(1 - (8/3)K_1)$ times the maximum stable timestep for the standard Yee method. The dispersion relation is plotted for the case $K_1 = -1/8$, $K_2 = 0$ and $\Delta_x = \Delta_y = \Delta_z = \Delta$ in Fig. 4. In comparing Figs. 4 and 2, note that the situation in Fig. 4 is much improved. In Fig. 4, the $0.8c$ particles do not exceed the numerical propagation speed for most timesteps until just before the grid cuts off the propagation. Note that the grid cut off point in any direction corresponds the point where the dispersion curves reach their maximum and start to decrease. As K_1 becomes more negative, the situation improves even more, as demonstrated by Fig. 5. Note, however, that as K_1 becomes more negative, the maximum stable timestep also decreases. Similar behavior is observed for the $K_2 = 2K_1$ case, as shown in Figs. 6 and 7.

Although the extended computational stencils to approximate the curl operator effectively eliminate the numerical Cerenkov radiation, major difficulties remain a hindrance to their practical implementation within a PIC code. First, it is difficult to find a particle current weighting scheme that is charge conserving within the extended computational framework. Second, the extended stencils are problematic near material boundaries boundaries in the grid. The stencil must be modified near a boundary, and this has ramifications on charge conservation and current weighting. Because of these difficult implementation issues, filtering schemes are much more commonly used to eliminate numerical Cerenkov radiation.

4. Filtering

The Fourier transform is used to understand filtering schemes to eliminate numerical Cerenkov radiation. After taking the Fourier transform in space and time, Maxwell's curl equations (Eq. (1)) become:

$$\begin{aligned} \omega\tilde{\mathbf{B}} &= \mathbf{k} \times \tilde{\mathbf{E}}, \\ \omega\tilde{\mathbf{E}} &= -c^2\mathbf{k} \times \tilde{\mathbf{B}} - i\eta c\tilde{\mathbf{J}}. \end{aligned} \tag{9}$$

If a filter $H_e(\omega)$ is applied to the electric field and a filter $H_b(\omega)$ is applied to the magnetic flux density, these equations become:

$$\begin{aligned} \omega H_b(\omega)\tilde{\mathbf{B}} &= \mathbf{k}\times\tilde{\mathbf{E}}, \\ \omega H_e(\omega)\tilde{\mathbf{E}} &= -c^2\mathbf{k}\times\tilde{\mathbf{B}} - i\eta c\tilde{\mathbf{J}}. \end{aligned} \tag{10}$$

The corresponding dispersion relation becomes

$$\frac{\omega^2}{H_b(\omega)H_e(\omega)c^2} = k_x^2 + k_y^2 + k_z^2 = k^2 \tag{11}$$

and the approximate dispersion relation in the Yee FDTD method becomes

$$\frac{1}{H_b(\omega)H_e(\omega)c^2\Delta_t^2}\sin^2\left(\frac{\omega\Delta_t}{2}\right) = \left[\frac{1}{\Delta_x}\sin\left(\frac{k_x\Delta_x}{2}\right)\right]^2 + \left[\frac{1}{\Delta_y}\sin\left(\frac{k_y\Delta_x}{2}\right)\right]^2 + \left[\frac{1}{\Delta_z}\sin\left(\frac{k_z\Delta_x}{2}\right)\right]^2. \tag{12}$$

In examining Eqs. (11) and (12), it is apparent that the magnitude of the filter alters the wave propagation speed and the phase of the filter introduces an imaginary part of ω which, depending on its sign, corresponds to amplification or attenuation. Note that the magnitude response of the filter also impacts the maximum stable timestep. Qualitatively, the maximum stable timestep must limit the propagation distance of any wave that can exist on the numerical grid to one cell in a timestep. Thus, filters whose magnitude response is greater than unity require a reduction in the maximum timestep while filters whose magnitude response is less than unity may allow an increase in the maximum stable timestep. Note that in cases where a single filter is applied, the filter can be equivalently applied either to **E** or **B**.

Ideally, the value of the filter should be unity (with zero phase) at low frequency so as not to affect the physics of interest in the simulation. The goal of filtering schemes is to attenuate high-frequency waves that may propagate slower than the high-energy particles in the simulation and cause numerical Cerenkov radiation. This must be accomplished through the phase response of the filter. Thus, the ideal filter is an all pass filter (magnitude response 1) with zero phase response at low frequency that becomes large at high frequency to attenuate the poorly resolved frequencies that propagate too slowly and cause numerical Cerenkov radiation. An example of such a response is shown in Fig. 8.

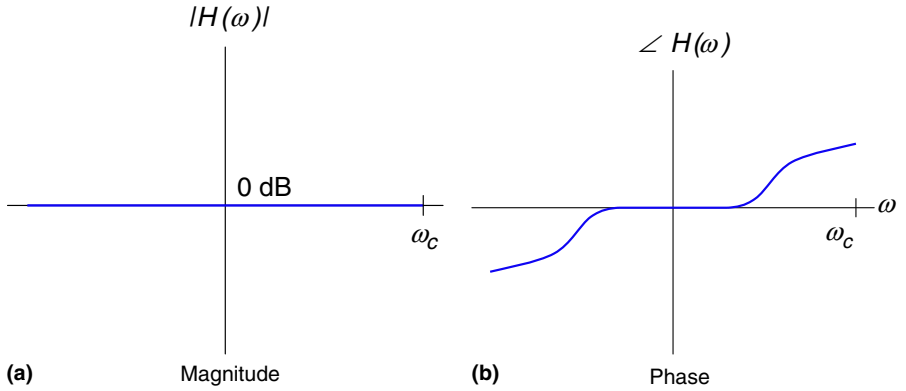

Fig. 8. Ideal filter response for elimination of numerical Cerenkov radiation.

4.1. Godfrey filter

Attention is now turned to two previously published filtering schemes. The scheme published by Godfrey [4] uses the standard Yee update equation for the magnetic flux density and the following update equation for the electric field:

$$\mathbf{E}^{n+1} = \mathbf{E}^{n} + c^2 \Delta_t \nabla \times \left(\alpha_1 \mathbf{B}^{n+3/2} + \alpha_2 \mathbf{B}^{n+1/2} + \alpha_3 \mathbf{B}^{n-1/2}\right), \tag{13}$$

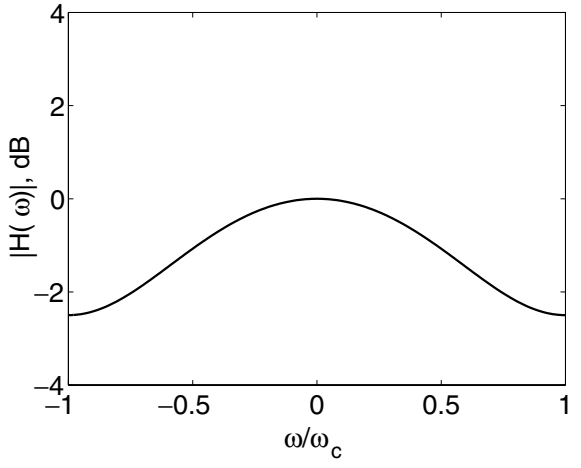

Filter magnitude

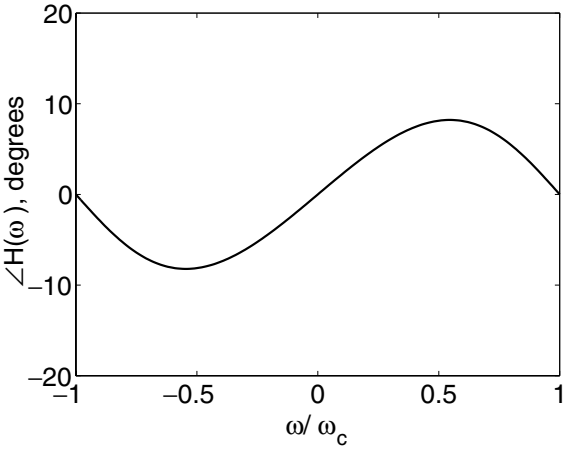

Filter phase

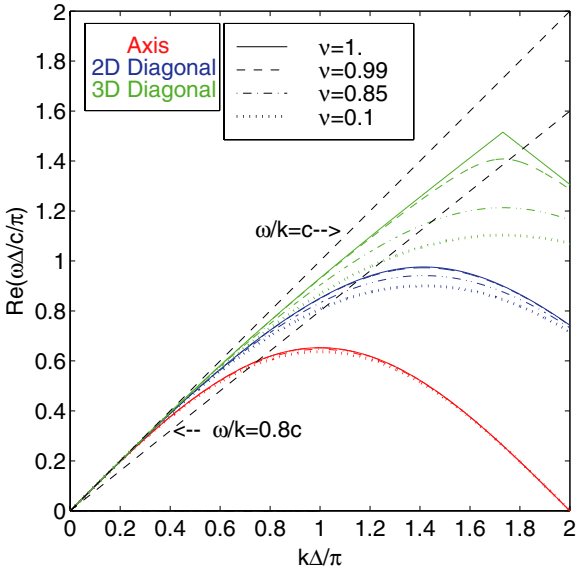

Dispersion real part

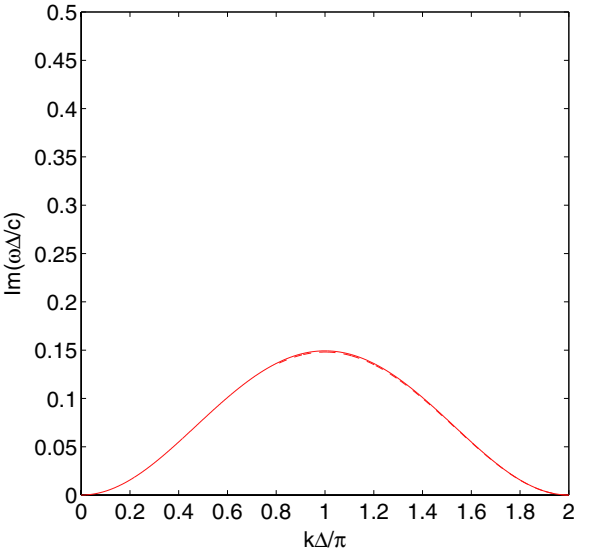

where the superscript n indicates the quantity evaluated at $t = n\Delta_t$ and $\alpha_1 + \alpha_2 + \alpha_3 = 1$. This corresponds to a filter $H_b(\omega) = \alpha_1 e^{j\omega\Delta_t} + \alpha_2 + \alpha_3 e^{-j\omega\Delta_t}$ with $H_e(\omega) = 1$. Note that the filter is non-causal if α_1 is non-zero and that the standard Yee scheme is recovered when $\alpha_1 = \alpha_3 = 0$ and $\alpha_2 = 1$. In [4], an iterative relaxation scheme is suggested for including the non-causal term.

The Godfrey filter is commonly used with $\alpha_3 = 0$. In this mode, the filter response is low-pass as shown in Fig. 9(a). Note that this filter deviates from the ideally desired response in important ways. First, the low-pass response of the filter slows the wave propagation at high frequency even further than the standard Yee scheme. However, the slower propagation allows the maximum timestep to be in-

Fig. 10. Response of the Godfrey filter and corresponding filtered FDTD dispersion relation with $\alpha_1 = 0$, $\alpha_2 = 1.1$, $\alpha_3 = -0.1$. The Nyquist cut off frequency for the filter is ω_c, and for the dispersion relation $\Delta_x = \Delta_y = \Delta_z = \Delta$ and $\Delta_t = v\Delta_{t,\max} = (10/11)v\Delta/c/\sqrt{3}$.

creased (by a factor of $1/\sqrt{\alpha_2^2 - 4\alpha_1\alpha_3}$), partially compensating for the increased computation time required by the iterative relaxation scheme. Second, the phase of the filter is linearly increasing near $\omega = 0$, meaning that wave propagation is attenuated at all frequencies, including the frequencies of physical interest. The dispersion relation for the Yee FDTD method with the filter of Fig. 9(a) and (b) is shown in Fig. 9(c) and (d). In comparing Fig. 9(c) to Fig. 2, note the slower wave propagation in Fig. 9(c) at high frequency.

It is well known that shifting the impulse response of a filter leaves its magnitude response unchanged but multiplies its phase response by a factor of $e^{-j\omega t_0}$, where t_0 is the amount of time shift. Thus, if the Godfrey filter is shifted in time to make it causal, the sign of the phase response changes and the filter amplifies the high-frequency waves rather than attenuating them. A causal Godfrey filter can be created, however, by setting $\alpha_1 = 0$ and $\alpha_3 < 0$. An example filter response and corresponding dispersion relation are shown in Fig. 10. The magnitude of the filter is now larger than unity at high frequency, corresponding to an increase in the high-frequency propagation speed. This results in a reduction in the maximum stable timestep by a factor of $1/\sqrt{\alpha_2^2 - 4\alpha_1\alpha_3}$, but since the filter is causal, the iterative relaxation scheme is no longer required. Note that the filter still attenuates propagation at all frequencies.

4.2. Friedman filter

The scheme published by Friedman [5] and Rambo et al. [6] uses the standard Yee update equation for **E** and the following update equation for **B**:

$$\mathbf{B}^{n+1/2} = \mathbf{B}^{n-1/2} - \Delta_t \nabla \times \left[\left(1 + \frac{\theta}{2}\right)\mathbf{E}^n - \theta\left(1 - \frac{\theta}{2}\right)\mathbf{E}^{n-1} + \frac{1}{2}(1-\theta)^2\theta\bar{\mathbf{E}}^{n-2} \right], \tag{14}$$

where

$$\bar{\mathbf{E}}^{n-2} = \mathbf{E}^{n-2} + \theta\bar{\mathbf{E}}^{n-3} \tag{15}$$

and $0 \leqslant \theta \leqslant 1$. Note that the standard Yee scheme is recovered when $\theta = 0$.

In contrast to the Godfrey scheme, which employs a finite impulse response (FIR) filter, the Friedman scheme employs an infinite impulse response (IIR) filter. The impulse response is given by

$$h_e[n] = \begin{cases} 0, & n < 0, \\ 1 + \theta/2, & n = 0, \\ -\theta(1 - \theta/2), & n = 1, \\ \left[(1-\theta)^2\theta^{n-1}\right]/2, & n > 1. \end{cases} \tag{16}$$

Note that because $h_e[n] = 0$ for all $n < 0$, the filter is causal, which greatly simplifies its implementation. The frequency response of the filter is given by

$$H_e(\omega) = 1 - \frac{2\theta\sin^2(\omega\Delta_t/2)}{e^{j\omega\Delta_t} - \theta}. \tag{17}$$

The maximum timestep for the FDTD scheme with the Friedman filter is somewhat problematic to derive. Assuming a Fourier mode solution of the form

$$\begin{bmatrix} \mathbf{E}(I\Delta_x, J\Delta_y, K\Delta_z, n\Delta_t) \\ \mathbf{B}(I\Delta_x, J\Delta_y, K\Delta_z, n\Delta_t) \end{bmatrix} = \begin{bmatrix} \mathbf{E}_0 \\ \mathbf{B}_0 \end{bmatrix} G^n e^{i(Ik_x\Delta_x + Jk_y\Delta_y + Kk_z\Delta_z)}, \tag{18}$$

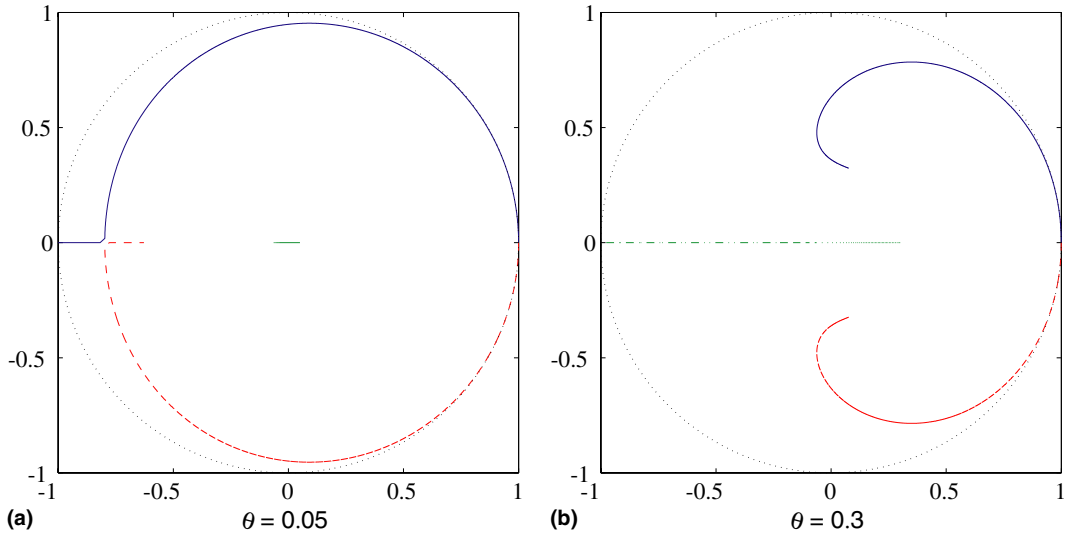

Fig. 11. Root locus of Eq. (19) for two values of θ when f varied from 0 to $\sqrt{(1+\theta)/(1+3\theta)}$.

a stable scheme requires $|G| \leqslant |$. It can be shown that G satisfies:

$$G^3 + (2+\theta)(2f^2-1)G^2 + [1+2\theta(1-4f^2)]G + \theta(2f^2-1) = 0, \tag{19}$$

$$f = c\Delta_t \sqrt{\left[\frac{\sin(k_x\Delta_x/2)}{\Delta_x}\right]^2 + \left[\frac{\sin(k_y\Delta_x/2)}{\Delta_y}\right]^2 + \left[\frac{\sin(k_z\Delta_x/2)}{\Delta_z}\right]^2}. \tag{20}$$

The magnitude of the roots of Eq. (19) is bounded by 1 if $f \leqslant \sqrt{(1+\theta)/(1+3\theta)}$. An upper bound is then placed on Δ_t by noting that the maximum value of the quantity under the radical in Eq. (20) is $1/\Delta_x^2 + 1/\Delta_y^2 + 1/\Delta_z^2$. While this limit on Δ_t is sufficient to prevent the numerical solution from growing without bound, the behavior of the scheme changes dramatically at a practical limit slightly lower than the stability limit. This can be seen by examining the root locus plots of Fig. 11. When the complex roots shown in red and blue are on the unit circle, there is no damping in the scheme. For higher frequency waves, these roots are inside the unit circle, indicating high-frequency damping in the scheme. For $\theta < 0.1168$ or $\theta > 1/2$, there is a point where these two roots become real and equal (see Fig. 11(a)) and the behavior of the scheme changes. Eq. (19) has at least two equal roots when

$$4\theta(\theta+2)^2(3\theta-2)(f^2)^3 - 8\theta(2\theta^3-5\theta^2+11\theta-6)(f^2)^2 + (\theta-1)^2(7\theta^2-16\theta+1)f^2 - (\theta-1)^4 = 0. \tag{21}$$

For $0.1168 < \theta < 1/2$, no real values of f satisfy Eq. (21), and Eq. (19) never has two equal roots. In this case, Fig. 11(b) shows the situation, and the behavior of the scheme changes when the real parts of all three roots of Eq. (19) are equal, which occurs when

$$(2f^2-1)[4(\theta+2)^3(f^2)^2 - 4(\theta+2)(\theta-1)(\theta-4)f^2 + (\theta-1)^2] = 0. \tag{22}$$

Values of f^2 that satisfy Eq. (21) can be found by defining

$$\begin{aligned} p &= -\tfrac{8\theta(2\theta^3-5\theta^2+11\theta-6)}{4\theta(\theta+2)^2(3\theta-2)}, & a &= \tfrac{1}{3}(3q-p^2),\\ q &= \tfrac{(\theta-1)^2(7\theta^2-16\theta+1)}{4\theta(\theta+2)^2(3\theta-2)}, & b &= \tfrac{1}{27}(2p^3-9pq+27r),\\ r &= -\tfrac{(\theta-1)^4}{4\theta(\theta+2)^2(3\theta-2)}, & c &= 2\sqrt{-\tfrac{a}{3}},\\ \Psi &= \tfrac{1}{3}\mathrm{Arccos}\left(\tfrac{3b}{ac}\right). \end{aligned} \tag{23}$$

The roots of Eq. (21) are then given by

$$f_k^2 = c\cos\left(\Psi + \frac{2(k-1)\pi}{3}\right) - \frac{p}{3}, \tag{24}$$

where $k = 1, 2, 3$. When $0 < \theta < 0.1168$ or $1/2 < \theta < 2/3$, f_3 corresponds to the practical limit, and when $2/3 < \theta < 1$, f_1 corresponds to the practical limit. At $\theta = 2/3$, both f_1 and f_3 are discontinuous, and the practical limit is easily found by noting that Eq. (21) reduces to a quadratic equation in f^2. When $0.1168 < \theta < 1/2$, a root of Eq. (22) corresponds to the practical limit, which is found to be

$$f^2_{\text{prac lim}} = \begin{cases} \frac{\theta-1}{2(\theta+2)^2}\left(\theta - 4 - 3\sqrt{2-\theta}\right), & 0.1168 < \theta < 0.3028,\\ \frac{1}{2}, & 0.3028 < \theta < 1/2. \end{cases} \tag{25}$$

Most of the expressions for the practical limit are somewhat cumbersome to use; thus, a plot showing the practical and stability limits is shown in Fig. 12. Once the practical limit on f is found, the corresponding timestep is given by

$$\Delta_{t,\text{prac lim}} = \frac{f_{\text{prac lim}}}{c\sqrt{1/\Delta_x^2 + 1/\Delta_y^2 + 1/\Delta_z^2}}. \tag{26}$$

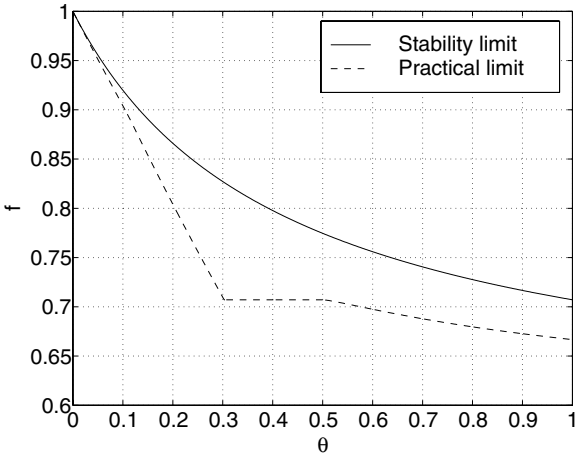

Fig. 12. Comparison of the stability limit of the FDTD method with the Friedman filter with the practical limit.

Note that running the scheme between the practical limit and the stability limit does not result in a divergent solution. However, physically undesirable behavior can result in this region, which is discussed in connection with the FDTD dispersion relations below.

The Friedman filter frequency response and corresponding FDTD dispersion relation for $\theta = 0.05$ are shown in Fig. 13. Note that the phase of the filter response is very close to the ideal response shown in Fig. 8, which is characterized by flat, zero phase at low frequency and increasing phase leading to attenuation as the frequency increases. The magnitude of the filter response is characterized by a small ripple

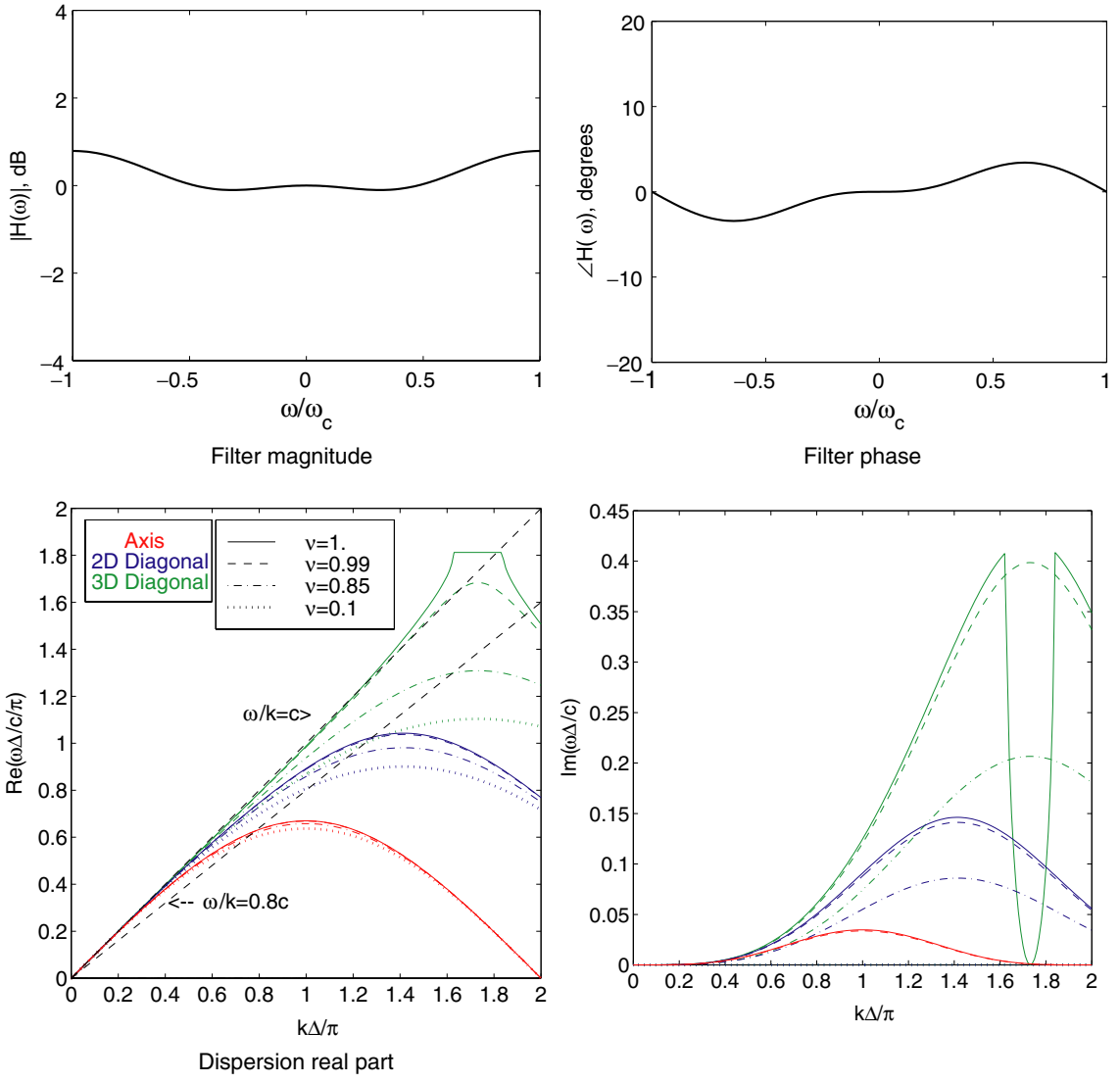

and increasing amplitude at high frequency. This is consistent with maximum timestep for the scheme being slightly smaller that the maximum timestep for the unfiltered Yee scheme. If the scheme is run at the stability limit, Fig. 13(d) shows that just before the 3D diagonal wave number cutoff at $k\Delta = \pi\sqrt{3}$, the imaginary part of the dispersion relation (and correspondingly the damping in the scheme) goes abruptly to zero. This corresponds with the roots shown in red and blue in Fig. 11(a) becoming real and equal before the stability limit. If the scheme is run at or below the practical limit (corresponding to $v = 0.9954$), this undesirable behavior disappears. As a second example, the filter frequency response and corresponding FDTD dispersion relation for $\theta = 0.3$ are shown in Fig. 14. In

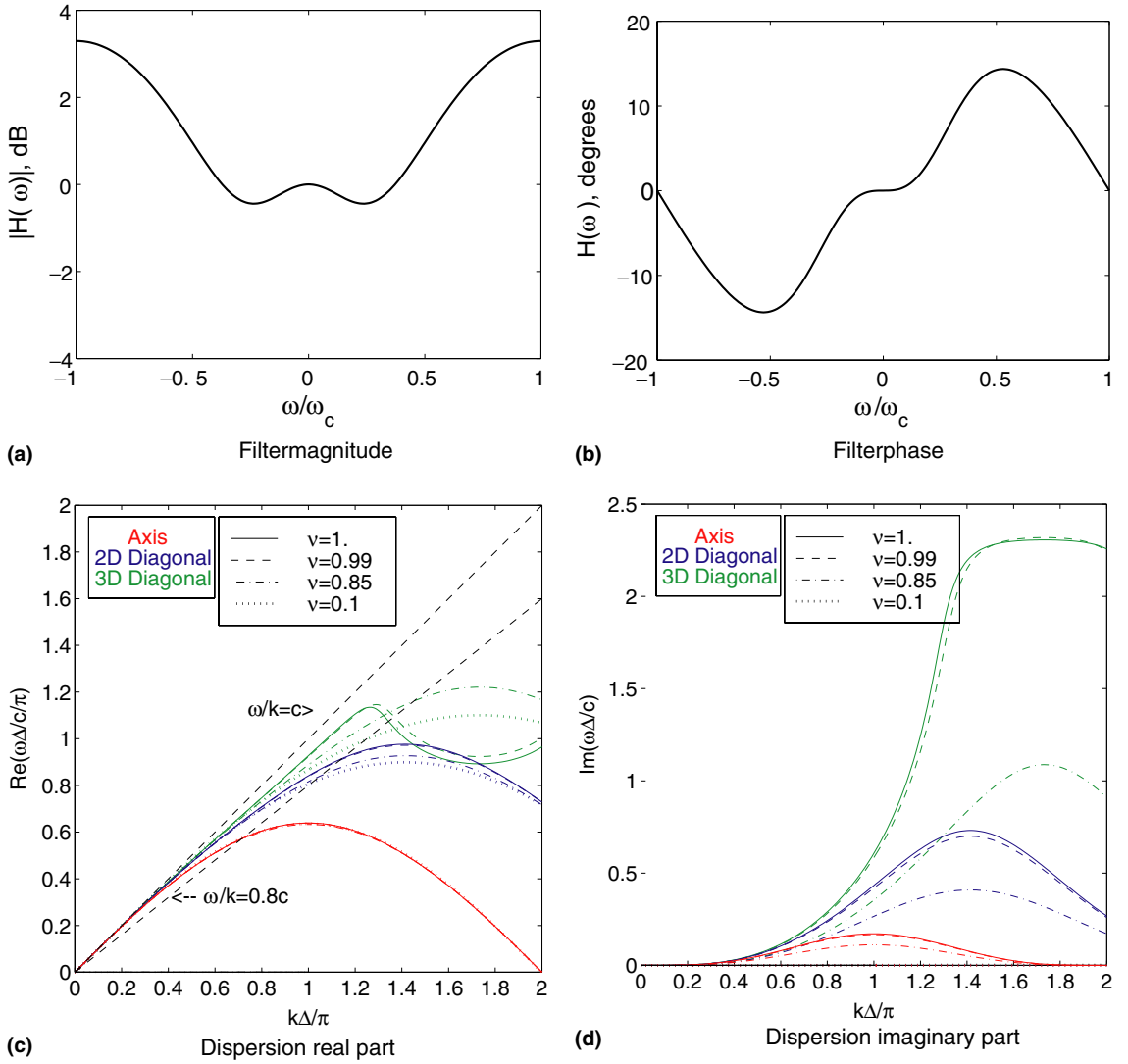

Fig. 14. Response of the Friedman filter and corresponding filtered FDTD dispersion relation with $\theta = 0.3$. The Nyquist cut off frequency for the filter is ω_c, and for the dispersion relation $\Delta_x = \Delta_y = \Delta_z = \Delta$ and $\Delta_t = v\Delta_{t,\max} = 0.8272v\Delta/c/\sqrt{3}$. The practical timestep limit is at $v = 0.8579$.

comparing Figs. 13 and 14, note that the magnitude and phase response of the filter keep approximately the same shape but vary in amplitude as θ is varied. In Fig. 14(c), note that if the scheme is run at the stability limit, the real dispersion curve corresponding to wave propagation along a 3D grid diagonal peaks and begins to decrease well before its wave number cutoff at $k\Delta = \pi\sqrt{3}$. This corresponds with the roots shown in red and blue in Fig. 11(b) curling around so their real parts begin increasing. Similar to the $\theta = 0.05$ case, if the scheme is run at or below the practical limit, the undesirable behavior disappears. For $\theta = 0.3$, the practical limit corresponds to $f = 0.7096$ which is $v = 0.8579$.

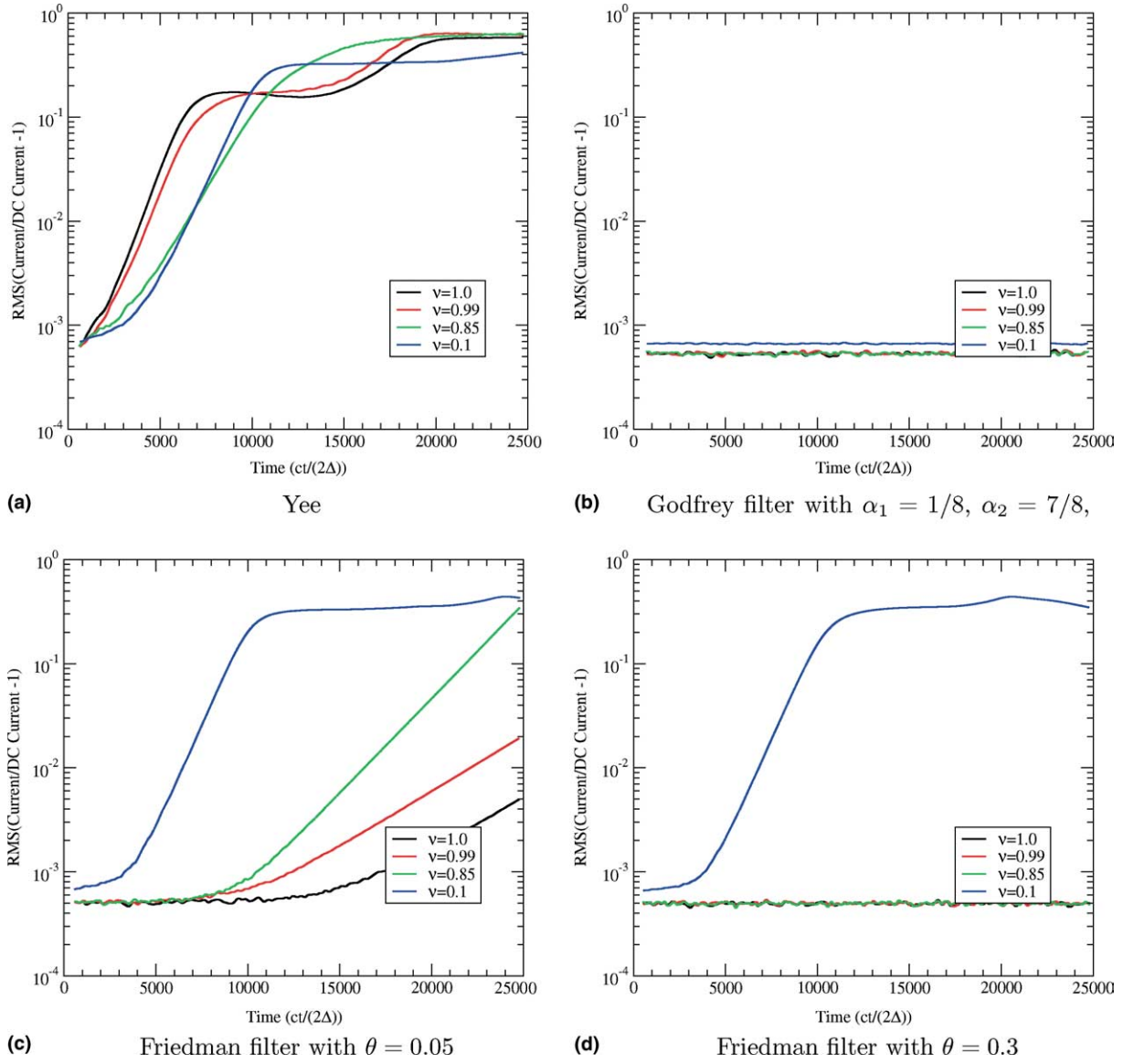

Fig. 15. RMS value of the oscillating current (in the z-direction) at the center of the cylinder for each simulation. The numerical filtering corresponds to the numerical dispersion diagrams shown in Figs. 2, 9, 13, and 14.

4.3. Numerical filter examples

The effects of the different filtering schemes on a physical problem are now shown. The problem is a right circular cylinder with a radius of 5 cm and a length of 10 cm. A 100 Ampere beam of 5 mm radius moves directly down the center of the cylinder at a velocity of $0.8c$. An axial magnetic field of 1 T is included in the simulations to remove the fire-hose instability. A sausage like instability still exists in this configuration, and the instability growth rate is affected by the simulation filtering scheme.

The simulations are executed with the same numerical parameters used to produce the numerical dispersion relations shown in Figs. 2, 9, 13, and 14. Note that the beam velocity is also shown in these figures. For each simulation, the RMS value of the oscillating current (in the z-direction) at the center of the cylinder is shown in Fig. 15. An intuitive understanding of the filtering methods is gained by comparing the current oscillations in Fig. 15 to the damping shown in the dispersion diagrams in Figs. 2, 9, 13, and 14.

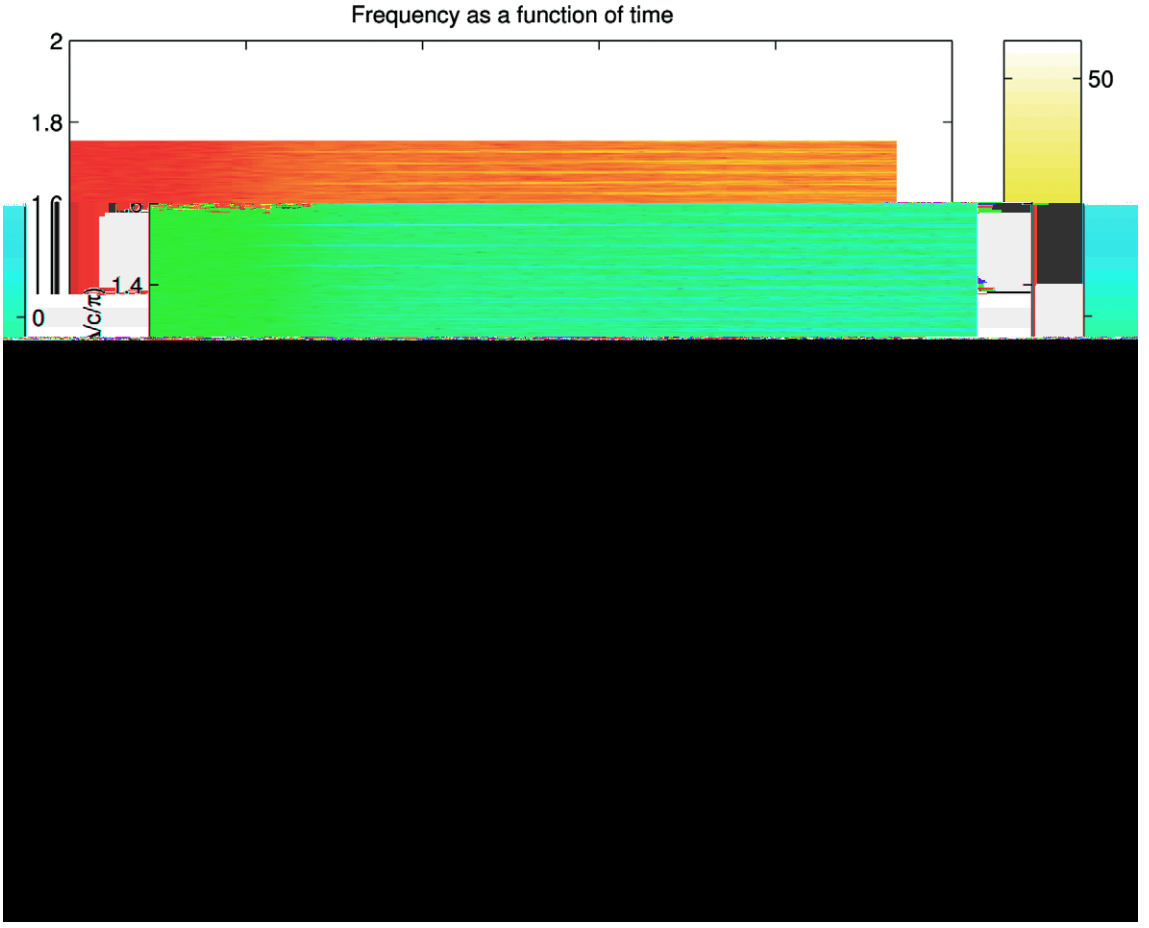

Fig. 16. A windowed Fourier transform of the current from a simulation using the Yee algorithm with $v = 0.99$. The fast growth of numerical modes at normalized frequencies around one and a late time white noise spectrum are shown. The amplitude (color) in this figure is plotted on a logarithmic scale.

Focusing first on the unfiltered or standard Yee simulation, note that all the curves go though two growth regions. The first is fast growing numerical Cerenkov radiation. In Fig. 16, the data from the $v = 0.99$ simulation is shown with a windowed Fourier transform, and the fast growth of these modes is noted at normalized frequencies around one. The amplitude (color) in the figure is plotted on a logarithmic scale. The dispersion diagram in Fig. 2 shows that the group velocity of these frequencies are near zero and therefore the modes are not moving. Thus, these modes are stationary and are not convected away. The second growth region is a complete break up of the beam. On the right hand side of Fig. 16 note that most frequencies are excited resulting in an almost white noise spectrum. The amplitude of the RMS current oscillations in Fig. 15 is close to the amplitude of the initial injected direct current. This simulation is corrupted by the numerical Cerenkov radiation to the point that it has no bearing on physical reality.

When the simulation is run with a $\theta = 0.05$ Friedman filter and a timestep corresponding to $v = 0.85$, Fig. 17 shows that the high-frequency numerical modes are damped away. All simulations with $\theta = 0.05$ have enough damping that they do not go through the second growth region seen in the unfiltered case.

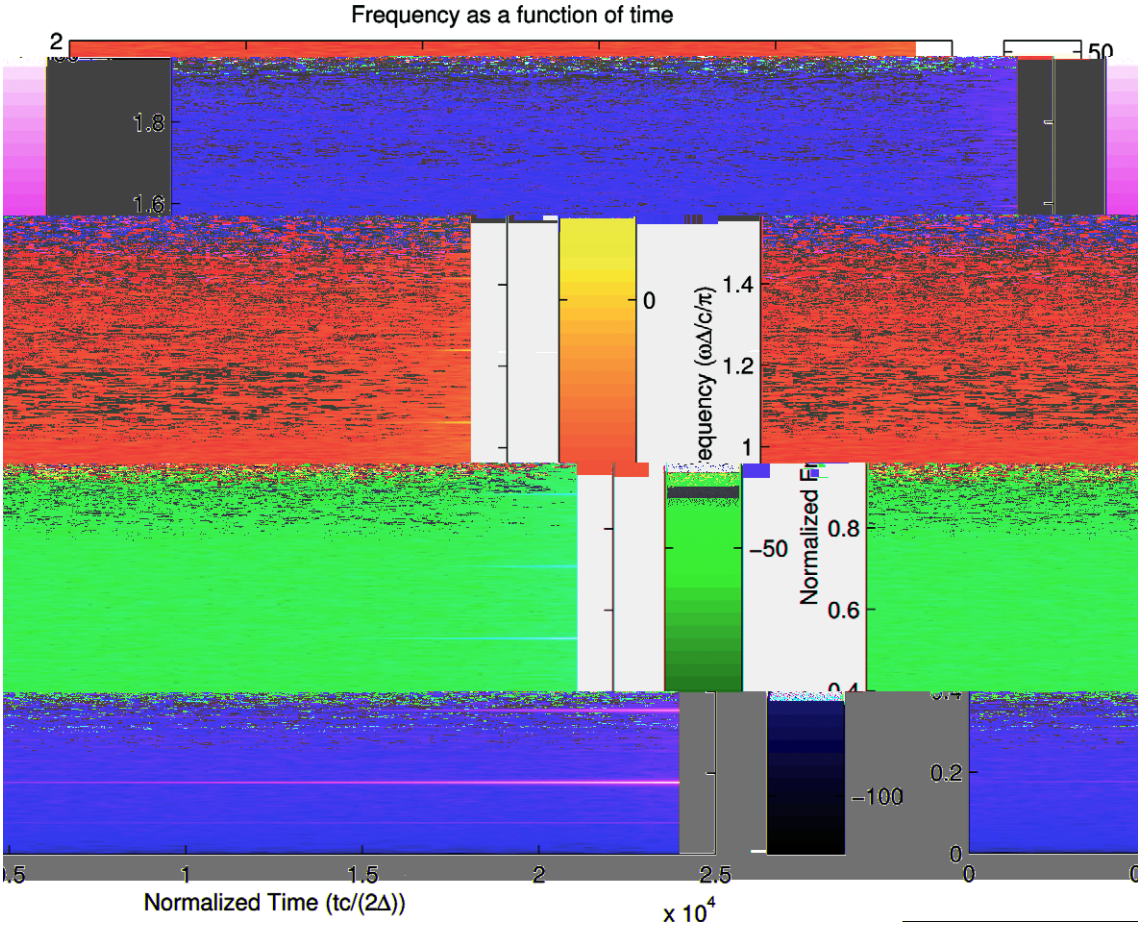

Fig. 17. A windowed Fourier transform of the current from a simulation using the Friedman filter with $\theta = 0.05$ and $v = 0.85$. The high-frequency numerical modes are damped away. The amplitude (color) in this figure is plotted on a logarithmic scale.

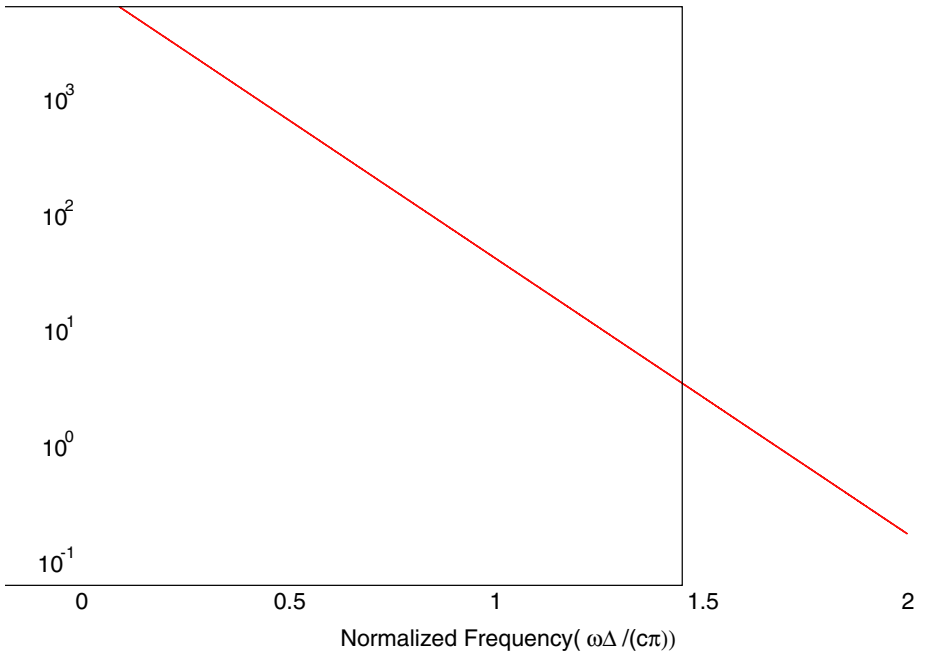

Fig. 18. A Fourier transform of the current from a simulation using the Friedman filter with $\theta = 0.05$ and $v = 0.85$. The high-frequency numerical modes are damped away and the remaining modes drop off exponentially.

The simulation of Fig. 17 still shows a sausage like mode that grows at a normalized frequency of 0.178. This mode is seen in the unfiltered case as well, but it is overwhelmed at late time. The 'sausage' mode is a wave-like density perturbation along the plasma column and is cylindrically symmetric about the column axis. The harmonics of the 'sausage' mode that are seen at late time drop off exponentially up to a normalized frequency of 1.3, as shown in Fig. 18. Note that a normalized frequency of 1.3 is the highest frequency supported by discretization in this simulation. In Fig. 15, note further that the 'sausage' growth rate is being altered by the Friedman filter as the Courant value is changed. The larger Courant values result in more damping. If simulation damping is increased even more by using a Friedman filter with $\theta = 0.3$ or a Godfrey filter with $\alpha_1 = 1/8$, $\alpha_2 = 7/8$, $\alpha_3 = 0$, then the 'sausage' instability is damped completely away with the exception of using the $\theta = 0.3$ Friedman filter with $v = 0.1$, which has the least damping of these cases. This example shows that these filters should not be used blindly. The physics of interest in a simulation should be at a frequency that is not significantly altered by the filter employed. In this respect, the Friedman filter is a better filter because the damping term has a zero slope going though the origin on the dispersion diagram, whereas the Godfrey filter has a damping term proportional to k near the origin. Thus, although the $\theta = 0.05$ Friedman filter and the $\alpha_1 = 1/8$, $\alpha_2 = 7/8$, $\alpha_3 = 0$ Godfrey filter have the same maximum damping, the Friedman filter shows the 'sausage' mode instability, but the Godfrey filter suppresses it.

5. Conclusion

Many PIC codes use the Yee FDTD method to model electromagnetic fields. This method is simple and robust, and a wealth of research is available from the computational electromagnetics community.

However, the Yee FDTD method also allows poorly resolved radiation near the grid cut off to propagate more slowly than the physical speed of light. When high-energy particles are present in the simulation, this leads to numerical Cerenkov radiation which corrupts the simulation. There are two methods of dealing with the numerical Cerenkov radiation: the problem can be eliminated by changing the computational stencil used to approximate the curl operator, and filtering can be introduced to attenuate the poorly resolved waves which cause the numerical Cerenkov radiation.

In examining different computational stencils for approximating the curl operator, it is found that stencils can be introduced which lead to numerical dispersion relations that eliminate the slowly traveling, poorly resolved radiation. However, these stencils are larger than the standard Yee computational stencil. Thus, boundary conditions and particle current weighting are extremely difficult to implement while maintaining a charge conserving numerical scheme. Thus, this method is not commonly used to eliminate numerical Cerenkov radiation.

Filtering schemes attempt to attenuate the poorly resolved high frequencies which lead to numerical Cerenkov radiation. When using filtering schemes, care must be taken not to alter the physics of interest in the numerical simulation. In examining the effect of filters on the wave dispersion relation, it is found that the ideal filter is characterized by an all pass magnitude response with zero phase in the frequency band of physical interest and increasing phase as the slowly traveling high frequencies near the grid cut off point are approached. Note that the ideal filter is not a low-pass filter.

The previously published scheme by Godfrey corresponds to a finite impulse response filter involving three samples. This filter is effective in eliminating numerical Cerenkov radiation, but because it is non causal it must be implemented using an iterative relaxation technique. The filter further has non-zero phase at all frequencies meaning that it attenuates radiation in the frequency band of physical interest.

The previously published scheme by Friedman corresponds to an infinite impulse response filter. The filter is causal and is characterized by a nearly ideal phase response. The magnitude response becomes larger than unity at high frequency, which increases the wave propagation speed at high frequency. This further reduces the numerical Cerenkov radiation but also requires a slight reduction in the maximum stable simulation timestep.

The derivation of the effect of filters on the wave dispersion relation contained in this paper allows filtering schemes to be analyzed and compared. It also leads to understanding of the ideally desired filter response. It is now possible to optimize filters to eliminate numerical Cerenkov radiation in PIC codes while preserving the physics of interest in the simulation.

References

[1] K.S. Yee, Numerical solution of initial boundary value problems involving Maxwell's equations in isotropic media, IEEE Trans. Antennas Propagat. 14 (1966) 302–307.
[2] C.K. Birdsall, A.B. Langdon, Plasma Physics via Computer Simulation, Adam Hilger, New York, 1991.
[3] R.W. Hockney, J.W. Eastwood, Computer Simulation Using Particles, McGraw-Hill, New York, 1981.
[4] B.B. Godfrey, Time-biased field solver for electromagnetic PIC codes, in: Proceedings of the Ninth Conference on Numerical Simulation of Plasmas, 1980.
[5] A. Friedman, Damped time advance methods for particles and EM fields, in: US–Japan Workshop on Advanced Computer Simulation Techniques Applied to Plasmas and Fusion, 1990.
[6] P. Rambo, J. Ambrosiano, A. Friedman, J.D.E. Nelson, Temporal and spatial filtering remedies for dispersion in electromagnetic particle codes, in: The 13th Conference on the Numerical Simulation of Plasmas, 1989.
[7] A. Friedman, A second order implicit particle mover with adjustable damping, J. Comput. Phys. 90 (1990) 292–312.
[8] M.F. Hadi, M. Picket-May, A modified (2,4) scheme for modeling electrically large structures with high phase accuracy, IEEE Trans. Antennas Propagat. 45 (1997) 254–264.